Supporting Information for High Electron Mobility and Insights into the Temperature-Dependent Scattering Mechanisms in InAsSb Nanowires

Jessica L. Boland,[†] Francesca Amaduzzi,[‡] Sabrina Sterzl,[†] Heidi Potts,[‡] Laura M Herz,[†] Anna Fontcuberta I Morral,[‡] and Michael B. Johnston[*,†]

[†]*Department of Physics, University of Oxford, Clarendon Laboratory, Parks Road, Oxford, OX1 3PU, United Kingdom*

[‡]*Laboratory of Semiconductor Materials, École Polytechnique Fédérale de Lausanne (EPFL), CH-1015 Lausanne, Switzerland*

E-mail: michael.johnston@physics.ox.ac.uk

Nanowire Growth and Crystal Structure

InAs and $InAs_{1-x}Sb_x$ nanowires were grown vertically on GaAs(111)B substrates via molecular beam epitaxy (MBE). The growth substrates were coated with a thin layer of silicon oxide of thickness 4.5 mm, and the growth was performed without a foreign catalyst. For all samples, the growth temperature was 520°C. InAsSb wires with different Sb content were obtained by changing the Sb flux while keeping all other growth parameters constant. The nanowires presented in this work have Sb concentrations of 0%, 11 %, 16%, 21% and 35% and diameters of 71±6 nm, 79±5 nm, 74±5 nm, 82±7 nm and 85±6 nm respectively. The length for all nanowires was found to be approximately 2 μm with a slight decrease with increased Sb content. Detailed information about the nanowire growth can be found in Ref.1.[1] All samples were then transferred to z-cut quartz discs for measurements.

High-resolution TEM analysis was carried out using a FEI Tecnai OSIRIS operated at 200 keV. All InAsSb and InAs nanowires were imaged in order to analyse the crystal structure as a function of Sb content for these NWs (Figure 1). All nanowires show a predominantly zinc blende (ZB) crystal structure with a varying density of stacking defects. For the reference sample with InAs nanowires, the defect density was extracted to be greater than 300 interfaces/μm, and especially at the nanowire stem Wurtzite (WZ) stacking can also be observed. For increasing Sb content, a strong decrease in defect density was observed, with defect densities of ∼220 interfaces/μm, ∼100 interfaces/μm and ∼1 interface/μm for InAsSb NWs with 16%, 21% and 35% Sb content, respectively. Above 16% Sb content, the WZ phase is completely suppressed and nanowires with 35% Sb content are almost completely defect-free with only a few twins per micrometre. A full discussion of the effect of Sb incorporation on the crystal structure can be found in Ref. 1.[1]

We would like to point out that the reported defect densities for nanowires with different Sb content correspond to an average value along the nanowires. However, especially for nanowires with intermediate Sb content, the defect density is not constant along the nanowires. The high-resolution TEM micrographs presented in the main article correspond

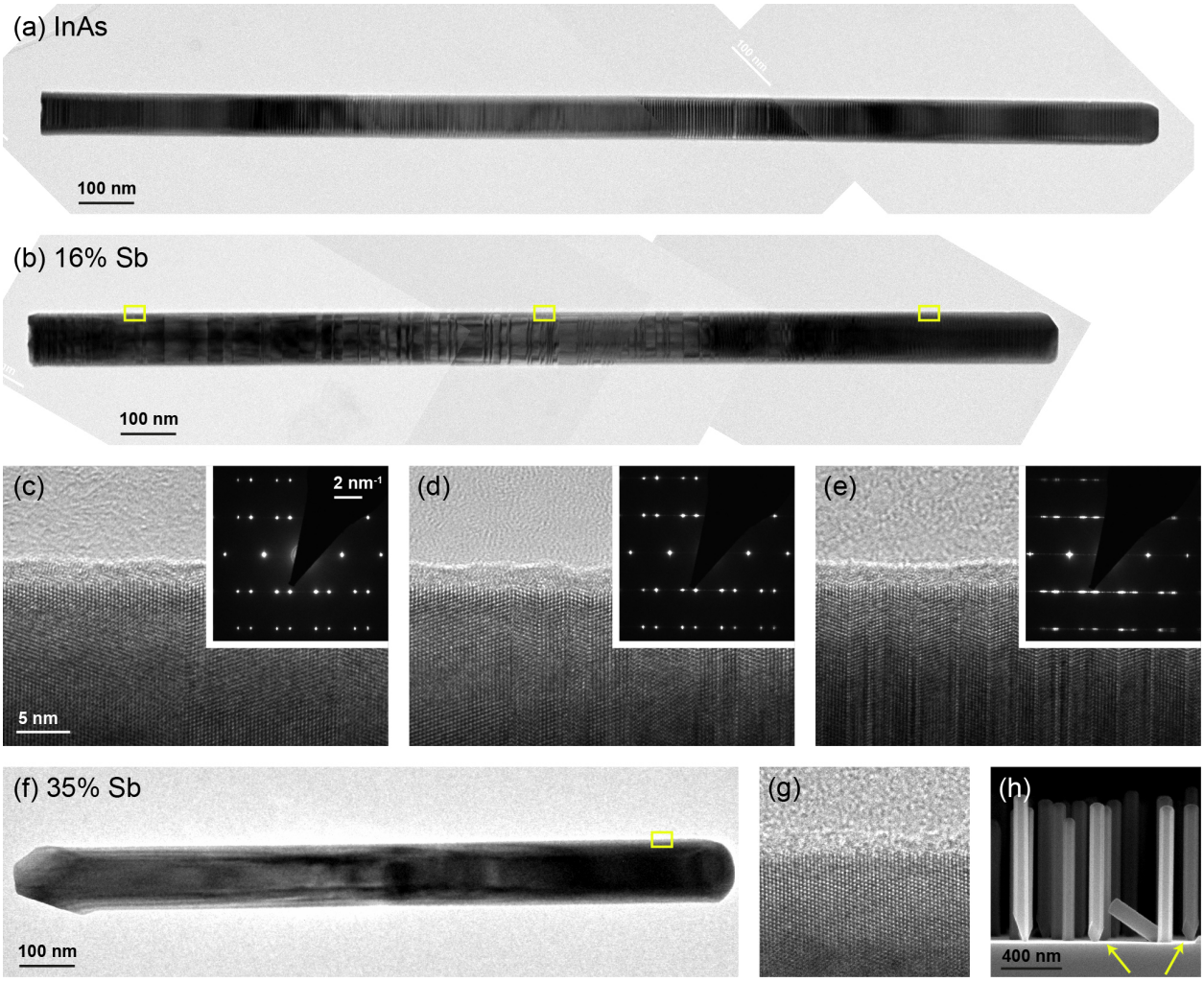

Figure 1: Crystal structure evolution along InAsSb nanowires. (a) TEM image of an InAs nanowire. (b) TEM image of an InAsSb nanowire with 16% Sb. (c)-(e) High resolution TEM images and selected area diffraction images at the nanowire stem, center and tip of 16% Sb nanowire. (f) TEM image of a 35% Sb nanowire. (g) High resolution TEM image at the tip of a 35% Sb nanowire. (h) Cross-sectional SEM image of the 35% Sb sample.

to the crystal structure in the middle of a nanowire. The full crystal structure evolution along nanowires with different Sb content is presented in Figure 1. Stacking defects can be observed by sharp changes in contrast perpendicular to the nanowire axis. Figure 1 (a) shows a TEM image of an InAs nanowire. The defect density is found to be roughly constant along the nanowire. Figure 1(b) shows a TEM image of an InAsSb nanowire with 16% Sb, and (c)-(e) show high-resolution TEM images and selected area diffraction images at the nanowire stem, center and tip, as indicated with yellow rectangles. The defect density is very low at the nanowire stem (a few defects per micrometre) and gradually increases along the nanowire. At the nanowire tip, the crystal structure is found to be similar to a pure InAs nanowires. The crystal structure evoluation along the nanowires explains the large variation in defect density which was reported in Ref. 1.[1] Figure 1(f) shows a TEM image of a nanowire with 35% Sb. The crystal structure is defect-free zinc-blende along the whole nanowire. A high resolution TEM image is shown in Figure 1(g). For completeness we note that at the stem of InAsSb nanowires with a high Sb content additional faceting is often observed. These facets can be explained by radial overgrowth and can be observed both in TEM and SEM images (highlighted by yellow arrows in Figure 1(h)).

Experimental Details for Infrared Photoluminescence Spectroscopy

Nanowires were photoexcited with a continuous-wave Ventus laser at a centre wavelength of 532 nm, at an average photoexcitation power of 2 mW. The beam path was focused onto the sample to produce a beam spot size of approximately 1.2 mm^2. The PL from the sample was then coupled into a Vertex 800V FTIR spectrometer using a gold parabolic mirror and an aperture of 8 mm. The PL signal was then detected via a liquid-nitrogen filled mercury cadmium telluride (MCT) detector at a resolution of 50 cm^{-1}. In order to spectral calibrate for the response of the FTIR spectrometer, a blackbody spectrum of the mid-infrared source within the FTIR was measured using the same settings as for the nanowire PL measurements. The theoretical blackbody curve for the intensity I was calculated using the following formula:

$$I = \frac{2\pi hc^2}{\lambda^5} \frac{1}{exp(\frac{hc}{\lambda k_B T}) - 1} \tag{1}$$

where h is the Planck constant, c the velocity of light and λ the wavelength. The Boltzmann constant is depicted by k_B and the temperature of the blackbody by T. The spectral response for calibrating the PL spectra is created by dividing the polynomial fit of the measured blackbody spectrum by these theoretical calculations. The PL spectra will be divided by this value to account for the sensitivity of the detector.

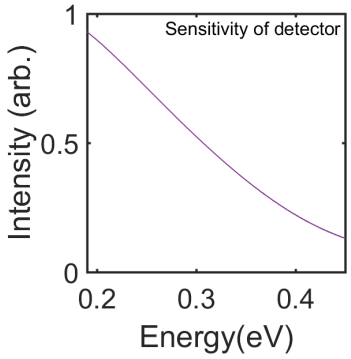

Figure 2: Sensitivity of the liquid-nitrogen filled mercury cadmium telluride detector of the measuring range.

As can be seen in figure Figure 2 the sensitivity of the MCT detector drastically decreases from 0.9 to 0.2 for 0.2 and 0.4 eV, respectively. This causes a lower signal-to-noise ratio which is detrimental to smaller signals.

Experimental Details for Raman Measurements

Raman measurements are done using the 488 nm line of Ar-Kr+ laser for excitation. The laser with power of 250 μW is focused on the single nanowire using a microscope objective with numerical aperture N.A.=0.75. The scattered light is collected by a TriVista spectrometer and detected by a CCD camera. The measurements are realized in back-scattering geometry with the nanowires suspended over a trench, in order to enhance the response of

the longitudinal optical phonon mode.[2] The temperature measurements are done by using a temperature controlled helium cryostat.

Data analysis for Raman measurements

The Raman lineshape of coupled mode can be evaluated using the dissipation fluctuation theorem. We have considered the standard dielectric theory in the formalism of Hon and Faust.[3] The differential Raman cross section from coupled phonon-plasmon modes of a doped two mode ternary alloy $A_xB_{1-x}C$ has the form:[4]

$$\frac{\partial^2\sigma}{\partial\omega\partial\Omega} \propto (n_\omega+1)I[\frac{-1}{\epsilon(\omega,x)}[\frac{1}{4\pi}+2\frac{A_1}{\epsilon_{\infty,1}}\chi_1(\omega,x)+2\frac{A_2}{\epsilon_{\infty,2}}\chi_2(\omega,x) \\ -4\pi(\frac{A_1}{\epsilon_{\infty,1}}-\frac{A_2}{\epsilon_{\infty,2}})^2\chi_1(\omega,x)\chi_2(\omega,x)-(1+\frac{4\pi}{\epsilon_\infty(x)}\chi_e(\omega))\epsilon_\infty(x)[(\frac{A_1}{\epsilon_{\infty,1}})^2\chi_1(\omega,x)+(\frac{A_2}{\epsilon_{\infty,2}})^2\chi_2(\omega,x)]] \tag{2}$$

where n_ω is the Bose-Einstein distribution, and $\epsilon(\omega,x)$ is the the dielectric function of the alloy and is given by:

$$\epsilon(\omega,x)=\epsilon_\infty(x)+4\pi(\chi_1(\omega,x)+\chi_2(\omega,x)+\chi_e(\omega)) \tag{3}$$

where $\epsilon_\infty(x)$ is the average high-frequency dielectric function and $\epsilon_\infty(x)x\epsilon_{\infty,1}+(1-x)\epsilon_{\infty,2}$. The i-sublattice contribution to the susceptibility is given by:

$$\chi_i(\omega,x)=x_i\frac{\epsilon_{\infty,i}}{4\pi}\frac{(\omega^0_{LO,i})^2-(\omega^0_{TO,i})^2}{(\omega^2_{TO,i}-\omega^2-i\omega\Gamma_i)} \tag{4}$$

where Γ_i is the phenomenological damping constant; $\omega^0_{TO,i}$ and $\omega^0_{LO,i}$ are the frequencies of TO and LO modes of the pure end-member compounds; $\omega_{TO,i}$ is the TO phonon

frequency of the alloy i-sublattice; χ_e the electronic susceptibility contribution; and $A_i = C_i^0 \frac{\omega_{TO,i}^2}{(\omega_{LO,i}^0)^2-(\omega_{TO,i}^2)^2}$ with C_i^0 is the Faust-Henry coefficient for the pure member compound.

We calculate the electronic susceptibility using the Hydrodynamical model, as follows[5] :

$$\chi_e = -\frac{\epsilon_\infty}{4\pi} \frac{\omega_p^2}{\omega^2 - < v^2 > q + i\omega\Gamma_e} \tag{5}$$

where ω_p is the plasma frequency ($\omega_p^2 = \frac{4\pi}{\epsilon_\infty} \frac{Ne^2}{m^*}$); Γ_ei s the damping constant related to the lifetime of the plasmon,$< v^2 >$ the electron mean square velocity and q the wavevector.

Considering the low band gap energy of InAsSb, we expect that the non-parabolicity of the conduction band is not negligible. For this reason, we use the Kane two band model to calculate the electronic dispersionl:[5]

$$E(k) = \frac{E_G}{2} \left[\sqrt{1 + \frac{4}{E_G} \frac{\hbar^2 k^2}{m^*}} - 1 \right] \tag{6}$$

Experimental Details for Optical Pump Terahertz Probe Spectroscopy

An amplified Ti:Sapphire laser with an average power of 4 W was used to generate 35 fs pulses centred at 800 nm at a repetition rate of 5 kHz. Each pulse was separated into three different paths: 590 μJ/pulse as an optical pump to photoexcite the sample; 200 μJ/pulse to generate the THz probe via optical rectification in a 2mm GaP crystal; and 1.6 μJ/pulse as a gate beam for electro-optical detection of the transmitted THz pulse via a 200 μm GaP crystal. In order to obtain a range of sample photoexcitation fluences between 5 μ J cm^{-2} to 26 μ J cm^{-2} , the optical pump beam was attenuated by neutral density filters. At the sample, the full width half maximum (FWHM) for the optical pump beam is 10 mm and for the THz

probe is 1 mm, so that the THz probe measures an area of homogenous photoexcited carrier density. The THz electric field, E, was measured using a balanced photodiode circuit and a lock-in amplifier referenced to a chopper at 2.5 kHz in the THz generation beam. The optical pump-induced change in the THz electric field, ΔE was measured using a second lock-in amplifier referenced to a chopper at 125 Hz in the optical pump beam. By varying the time delays between all three beams, a 2D map of the THz spectral response as a function of time after photoexcitation can then be measured. By also varying the power of the optical pump beam, a THz spectra response as a function of photoexcitation fluence can also be obtained. All measurements were taken at room temperature with the THz beam under vacuum to avoid any absorption of THz radiation by atmospheric water vapour.

Data Analysis of Terahertz Measurements

Extracting the Nanowire Equilibrium Conductivity

Terahertz time-domain spectroscopy (THz-TDS) measures the transmission function, $T(\omega)$, of the NWs, which is directly related to the NW conductivity at equilibrium, $\sigma(\omega)$, as well as the dielectric function, $\epsilon_{\mathrm{nw}}(\omega)$, and refractive index of the NWs, $\tilde{n}(\omega)$. To extract this equilibrium NW conductivity from the transmission function, the NW geometry and the nature of the EM wave propagation through the sample must be considered, as the characteristic dimensions of the NWs are much smaller than the diffraction-limited spot size of the incident THz probe pulse ($\sim$1 mm). An effective medium theory (EMT) is therefore necessary, where the NWs and surrounding medium are considered as a single composite layer, l, with an effective complex dielectric function, $\epsilon_{\mathrm{l}}(\omega)$, effective complex refractive index, $\tilde{n}_{\mathrm{l}}$, effective conductivity, $\sigma_{\mathrm{l}}(\omega)$ and effective thickness, d_{l}. For these measurements, the sample consists of a composite NW layer, which is supported by a quartz substrate of known complex refractive index, $\tilde{n}_{\mathrm{s}}$, and thickness, d_{s}. Within the composite layer, the NWs occupy a volume fraction, f, and the remainder of the volume is vacuum.

The theoretical expression for the transmission function, $T(\omega)$, can be derived by considering the Fresnel transmission and reflection of a wave propagating through the sample at normal incidence. For the geometry used in our work, the expression is given as:

$$\begin{aligned} T(\omega) &= \frac{E_{\mathrm{nw}}(\omega)}{E_{\mathrm{ref}}(\omega)} \\ &= \frac{2\tilde{n}_{\mathrm{l}}\left(\tilde{n}_{\mathrm{v}}+\tilde{n}_{\mathrm{s}}\right)}{\left(\tilde{n}_{\mathrm{v}}+\tilde{n}_{\mathrm{l}}\right)\left(\tilde{n}_{\mathrm{l}}+\tilde{n}_{\mathrm{s}}\right)} \exp\left(\frac{i\omega d_1}{c}\left(\tilde{n}_{\mathrm{l}}-\tilde{n}_{\mathrm{v}}\right)\right) \frac{FP_{\mathrm{vls}}FP_{\mathrm{lsv}}}{FP_{\mathrm{vsv}}}, \end{aligned} \tag{7}$$

where $\tilde{n}_{\mathrm{i}}$ are the frequency-dependent complex refractive indices, c is the speed of light in a vacuum and the subscripts v, l and s denote the vacuum, composite layer and substrate respectively. The Fabry-Pérot terms, FP_{ijk}, account for multiple internal reflections in the composite layer and substrate and are defined as:

$$FP_{\mathrm{ijk}} = \sum_{p=0}^{\mathrm{P}} \left(r_{\mathrm{jk}} r_{\mathrm{ji}} \exp\left(\frac{2i\tilde{n}_{\mathrm{j}}\omega d_{\mathrm{j}}}{c}\right)^{p}\right), \tag{8}$$

where $r_{\mathrm{ij}} = (\tilde{n}_{\mathrm{i}} - \tilde{n}_{\mathrm{j}})/(\tilde{n}_{\mathrm{i}} + \tilde{n}_{\mathrm{j}})$ are the Fresnel reflection coefficients. The summation limit P is set by the number of internal reflections recorded in the $E_{\mathrm{nw}}(t)$ and $E_{\mathrm{ref}}(t)$ waveforms.

Therefore, from the experimentally measured transmission function, $T(\omega)$ and the known properties of the surrounding media, the theoretical expression for $T(\omega)$ can be solved analytically to obtain $\tilde{n}_{\mathrm{l}}$ and the complex dielectric function of the composite layer, $\epsilon_{\mathrm{l}} = \tilde{n}_{\mathrm{l}}^2$. For NW samples, the composite layer is usually very thin in comparison to the wavelength of the THz radiation ($d_{\mathrm{l}} \ll \lambda_{\mathrm{THz}}$, $P \to \infty$) and the substrate is often very thick ($d_{\mathrm{s}} \geq \lambda_{\mathrm{THz}}$, $P = 0$), so that the expression or the transmission function can be simplified using the following approximations:

$$|\frac{\tilde{n}_{\mathrm{l}}\omega d_{\mathrm{l}}}{c}| \ll 1, \tag{9}$$

$$|\frac{\tilde{n}_{\mathrm{v}}\omega d_{\mathrm{l}}}{c}| \ll 1, \tag{10}$$

$$\exp\left(\frac{i\tilde{n}_{\mathrm{l}}\omega d_{\mathrm{l}}}{c}\right) = 1 + \frac{i\tilde{n}_{\mathrm{l}}\omega d_{\mathrm{l}}}{c} = 1, \tag{11}$$

$$FP_{\mathrm{lsv}} = 1, \tag{12}$$

$$FP_{\mathrm{vsv}}(\omega) = 1, \tag{13}$$

$$FP_{\mathrm{vls}} = \left(1 - r_{\mathrm{ls}}r_{\mathrm{lv}}\exp\left(\frac{2i\tilde{n}_{\mathrm{l}}\omega d_{\mathrm{l}}}{c}\right)\right)^{-1}. \tag{14}$$

By noting that the complex refractive index of the vacuum is $\tilde{\mathrm{n}}_{\mathrm{v}} = 1$ and applying these approximations, the transmission function becomes:

$$T(\omega) = \frac{(1+\tilde{n}_{\mathrm{s}})}{(1+\tilde{n}_{\mathrm{s}}) - \dfrac{i\omega d_{\mathrm{l}}\left(\tilde{n}_{\mathrm{s}}^2 + \tilde{n}_{\mathrm{s}}\right)}{c}}. \tag{15}$$

By rearranging this transmission function and substituting $\epsilon_{\mathrm{l}} = \tilde{n}_{\mathrm{l}}^2$, the effective complex dielectric function of the composite layer can be calculated:

$$\epsilon_{\mathrm{l}} = \frac{ic(1+\tilde{n}_{\mathrm{s}})}{\omega_l}\left(\frac{1}{T(\omega)} - 1\right) - \tilde{n}_{\mathrm{s}}. \tag{16}$$

Once the complex dielectric function, ϵ_{l}, is determined, $\epsilon_{\mathrm{l}} = \epsilon_{\mathrm{L,l}} + i\sigma_{\mathrm{l}}/\omega\epsilon_0$ can then be used to extract the effective conductivity of the composite layer:

$$\sigma_{\mathrm{l}}(\omega) = \frac{\epsilon_0 c(1+\tilde{n}_{\mathrm{s}})}{d_{\mathrm{l}}}\left(\frac{1}{T(\omega)} - 1\right) + i\omega\epsilon_0(\tilde{n}_{\mathrm{s}} + \epsilon_{\mathrm{L,l}}(\omega)). \tag{17}$$

In the case of a highly conductive sample, this effective conductivity can be approximated to:

$$\sigma_{\mathrm{l}}(\omega) = \frac{\epsilon_0 c(1+\tilde{n}_{\mathrm{s}})}{d_1}\left(\frac{1}{T(\omega)} - 1\right). \tag{18}$$

Hence, from THz-TDS measurements, the effective conductivity of the NWs on substrate can be extracted from the experimental value of the THz transmission function.[6] However, it is important to note that to obtain the conductivity of the NWs alone ($\sigma(\omega)$) rather than the composite conductivity ($\sigma_{\mathrm{l}}(\omega)$), an appropriate effective medium theory (EMT) must be applied.

Extracting the Nanowire Photoconductivity

Optical-pump terahertz probe (OPTP) spectroscopy measures the relative photoinduced change in THz transmission, $\frac{\Delta T}{T}$, through the NW sample, which is directly related to the NW photoconductivity, $\Delta\sigma(\omega)$. Just as for the extraction of the NW equilibrium conductivity, calculation of the NW photoconductivity requires consideration of the sample geometry and the propagation of the THz pulse through the sample with and without photoexcitation, so an EMT must be used. Thus, the same sample geometry shown in[6] is used. Yet, in addition, the absorption depth of the photoexcitation pulse must also be taken into account. The substrate itself exhibits no photoconductivity response and the thin composite layer is uniformly photoexcited. By considering the wave propagation through the sample as before, a theoretical expression for $\frac{\Delta T}{T}$ can be derived:

$$\begin{aligned}\frac{\Delta T(\omega)}{T(\omega)} &= \frac{E_{\mathrm{nw}}^{\mathrm{ON}}(\omega)}{E_{\mathrm{nw}}^{\mathrm{OFF}}(\omega)} - 1 \\ &= \frac{(\tilde{n}_{\mathrm{v}} + \tilde{n}_{\mathrm{l}}^*)(\tilde{n}_{\mathrm{l}}^* + \tilde{n}_{\mathrm{s}})}{(\tilde{n}_{\mathrm{v}} + \tilde{n}_{\mathrm{l}})(\tilde{n}_{\mathrm{l}} + \tilde{n}_{\mathrm{s}})} \exp\left(\frac{i\omega d_{\mathrm{l}}}{c}(\tilde{n}_{\mathrm{l}}^* - \tilde{n}_{\mathrm{l}})\right) \frac{FP_{\mathrm{vls}}^* FP_{\mathrm{lsv}}^*}{FP_{\mathrm{vls}} FP_{\mathrm{lsv}}} - 1,\end{aligned} \tag{19}$$

where the superscript * denotes the values taken when the NWs are photoexcited. The experimentally measured $\frac{\Delta T}{T}$, as well as the known values of the thickness and refractive index of the substrate can then be substituted into this theoretical expression, leaving $\tilde{n}_{\mathrm{l}}^{*}$ and $\tilde{n}_{\mathrm{l}}$ as unknown. As again the NWs are much thinner than the THz wavelength ($d_{\mathrm{l}} \ll \lambda_{\mathrm{THz}}, P \rightarrow \infty$) and the underlying substrate is very thick ($d_{\mathrm{s}} \geq \lambda_{\mathrm{THz}}, P = 0$), the same approximations as outlined in Section 3.8.2 can be utilised to give the ratio of the photoinduced change in THz transmission to the THz transmission at equilibrium:

$$\frac{\Delta T(\omega)}{T(\omega)} = \frac{i\omega d_{\mathrm{l}}}{c} \frac{(\tilde{n}_{\mathrm{l}}^{*2} - \tilde{n}_{\mathrm{l}}^{2})}{(1 + \tilde{n}_{\mathrm{s}})}. \tag{20}$$

This ratio can be rearranged to give the photoinduced change in refractive index:

$$\tilde{n}_{\mathrm{l}}^{*2} - \tilde{n}_{\mathrm{l}}^{2} = -\frac{ic(1 + \tilde{n}_{\mathrm{s}})}{\omega d_{\mathrm{l}}} \frac{\Delta T(\omega)}{T(\omega)}. \tag{21}$$

This equation can be used to extract the complex dielectric function of the composite layer, as $\tilde{n}_{\mathrm{l}}^{*2} - \tilde{n}_{\mathrm{l}}^{2} = \epsilon_{\mathrm{l}}^{*} - \epsilon_{1}$. By utilising the definition, $\epsilon_{\mathrm{l}}^{*} - \epsilon_{\mathrm{l}} = i\Delta\sigma_{l}/\omega\epsilon_{0}$, the effective photoconductivity of the composite layer can then be determined:

$$\Delta\sigma_{\mathrm{l}}(\omega) = -\frac{\epsilon_{0} c(1 + \tilde{n}_{\mathrm{s}})}{d_{\mathrm{l}}} \frac{\Delta T(\omega)}{T(\omega)}. \tag{22}$$

The effective photoconductivity is therefore directly proportional to $\dfrac{\Delta T}{T}$, which is usually probed as a function of time after photoexcitation in OPTP studies. Thus, when examining how the experimentally measured $\dfrac{\Delta T}{T}$ changes with time after photoexcitation, the photoconductivity decay and thereby carrier dynamics of the NWs are being investigated. To extract the conductivity of the NWs alone, an appropriate EMT can again be applied and

the NW photoconductivity extracted as both a function of time after photoexcitation and frequency.[6]

Applying Effective Medium Theory

In order to extract both the equilibrium and photo-induced conductivities for the nanowires exactly, an effective medium theory must be applied. Here, we apply the Bruggeman effective medium theory, which takes the following form:

$$f\frac{\epsilon_{\mathrm{nw}}-\epsilon_{l}}{\epsilon_{\mathrm{nw}}+\kappa\epsilon_{\mathrm{l}}}+(1-f)\frac{\epsilon_{\mathrm{h}}-\epsilon_{\mathrm{l}}}{\epsilon_{h}+\kappa\epsilon_{\mathrm{l}}}=0. \tag{23}$$

This formula can be rearranged to solve for ϵ_{nw} in the following way:

$$\epsilon_{\mathrm{nw}}=\epsilon_{\mathrm{l}}\left(\frac{f(\epsilon_{\mathrm{h}}+\kappa\epsilon_{\mathrm{l}})-(1-f)\kappa(\epsilon_{\mathrm{h}}-\epsilon_{\mathrm{l}})}{f(\epsilon_{\mathrm{h}}+\kappa\epsilon_{\mathrm{l}})+(1-f)(\epsilon_{\mathrm{h}}-\epsilon_{\mathrm{l}})}\right). \tag{24}$$

In the above equation, κ is related to the depolarisation factor, which depends on the NW geometry and orientation relative to the electric field polarisation of the THz pulse: $\kappa = 2$ for spherical particles and $\kappa = 1$ for infinitely long cylinders oriented with their axes perpendicular to the THz electric field.

Although other EMTs that exist,[7] for analysis of the NW conductivity, both the Maxwell-Garnett and Bruggeman EMTs are the most appropriate, as they are derived considering the local depolarisation fields arising in NWs under the applied electric field. This provides a link to the plasmon model, which is similarly based on the depolarisation fields in semiconductor NWs. This link can therefore be exploited by considering the Maxwell-Garnet approximation for conducting and non-conducting NWs. In the non-conducting case, $\epsilon_{\mathrm{nw}} = \epsilon_{\mathrm{L,nw}}$ and $\epsilon_{\mathrm{l}} = \epsilon_{\mathrm{L,l}}$, so **??** becomes:

$$\epsilon_{\mathrm{L,l}} = \epsilon_{\mathrm{h}} \left(\frac{\kappa f(\epsilon_{\mathrm{L,nw}} - \epsilon_{\mathrm{h}}) + (\epsilon_{\mathrm{L,nw}} + \kappa\epsilon_{\mathrm{h}})}{-f(\epsilon_{\mathrm{L,nw}} - \epsilon_{\mathrm{h}}) + (\epsilon_{\mathrm{L,nw}} + \kappa\epsilon_{\mathrm{h}})} \right). \tag{25}$$

In the conducting case, $\epsilon_{\mathrm{nw}} = \epsilon_{\mathrm{L,nw}} + \dfrac{i\sigma}{\omega\epsilon_0}$ and $\epsilon_{\mathrm{l}} = \epsilon_{\mathrm{L,l}} + \dfrac{i\sigma_{\mathrm{l}}}{\omega\epsilon_0}$ and **??** becomes:

$$\epsilon_{L,l} + \frac{i\sigma_l}{\omega\epsilon_0} = \epsilon_{\mathrm{h}} \left(\frac{\kappa f(\epsilon_{\mathrm{L,nw}} + \dfrac{i\sigma}{\omega\epsilon_0} - \epsilon_{\mathrm{h}}) + (\epsilon_{\mathrm{L,nw}} + \dfrac{i\sigma}{\omega\epsilon_0} + \kappa\epsilon_{\mathrm{h}})}{-f(\epsilon_{\mathrm{L,nw}} + \dfrac{i\sigma}{\omega\epsilon_0} - \epsilon_{\mathrm{h}}) + (\epsilon_{\mathrm{L,nw}} + \dfrac{i\sigma}{\omega\epsilon_0} + \kappa\epsilon_{\mathrm{h}})} \right). \tag{26}$$

Combining Equation 25 and Equation 26 and solving for σ_{l}, gives:

$$\sigma_{\mathrm{l}}(\omega) = \frac{\dfrac{A}{B}\sigma_{\mathrm{nw}}}{B + (1-f)\dfrac{i\sigma_{\mathrm{nw}}}{\omega\epsilon_0}}, \tag{27}$$

where the constants A and B are defined as:

$$\begin{aligned} A &= f\epsilon_{\mathrm{h}}^2(\kappa+1)^2 \\ B &= -f(\epsilon_{\mathrm{L,nw}} - \epsilon_{\mathrm{h}}) + (\epsilon_{\mathrm{L,nw}} + \kappa\epsilon_{\mathrm{h}}) \end{aligned}. \tag{28}$$

Substituting in the Drude equation into Equation 27 gives:

$$\sigma_{\mathrm{l}}(\omega) = \frac{A}{B^2}\frac{Ne^2}{m^*}\frac{i\omega}{\omega^2 - \omega_0^2 + i\omega\gamma}, \tag{29}$$

where the resonant frequency is given by:

$$\omega_0 = \sqrt{\frac{(1-f)}{B}\frac{Ne^2}{m^*\epsilon_0}}. \tag{30}$$

Thus, the conductivity takes the same functional form as the plasmon response described earlier and the resonant frequency displays the same dependence on the $\sqrt{N}$ as for the plasmon response. From the conductivity expression of the composite layer, the equilibrium NW conductivity can be extracted:

$$\sigma_{\mathrm{nw}}(\omega) = \frac{B\sigma_l}{\frac{A}{B} - (1-f)\frac{i\sigma_{\mathrm{l}}}{\omega\epsilon_0}}. \tag{31}$$

Using the knowledge that $\Delta\sigma_{\mathrm{nw}} = \sigma^*_{\mathrm{nw}} - \sigma_{\mathrm{nw}}$, the following expression for the NW conductivity can then be derived:

$$\begin{aligned}\Delta\sigma_{\mathrm{nw}} &= \frac{B(\sigma_{\mathrm{l}} + \Delta\sigma_{\mathrm{l}})}{\frac{A}{B} - (1-f)\frac{i\sigma_{\mathrm{l}} + \Delta\sigma_{\mathrm{l}}}{\omega\epsilon_0}} - \frac{B\sigma_{\mathrm{l}}}{\frac{A}{B} - (1-f)\frac{i\sigma_{\mathrm{l}}}{\omega\epsilon_0}} \\ \Delta\sigma_{\mathrm{nw}} &= \frac{A\Delta\sigma_{\mathrm{l}}}{\left(\frac{A}{B} - (1-f)\frac{i(\Delta\sigma_{\mathrm{l}} + \sigma_{\mathrm{l}})}{\omega\epsilon_0}\right)\left(\frac{A}{B} - (1-f)\frac{i\sigma_l}{\omega\epsilon_0}\right)}\end{aligned}. \tag{32}$$

Extracting the Nanowire Transport Parameters

From the extracted photoinduced NW conductivity, several transport parameters can be extracted: the charge carrier density, carrier lifetime, surface recombination velocity, effective charge carrier mobility and mean free path. Firstly, the charge carrier density is directly related to the NW conductivity and can be obtained via the following equation:

$$n = \frac{2m*}{\pi e^2} \int_0^\infty \sigma_1(\omega)\, \mathrm{d}\omega, \tag{33}$$

where m^* is the effective mass of the charge carrier and e is the electronic charge. By probing how this carrier density changes with time after photoexcitation, the carrier lifetime can be determined by fitting the following carrier rate equation to the photoconductivity decay:

$$\frac{dn}{dt} = -\alpha n - \beta n^2 - \gamma n^3, \tag{34}$$

where α is the monomolecular recombination rate, β is the bimolecular radiative recombination rate and γ is the Auger recombination constant. For materials that are known to exhibit surface trapping, measurement of the photoconductivity decay for NWs of different diameters can determine the surface recombination velocity. The NW geometry is approximated as a cylinder of infinite length and a continuity equation describing the carrier concentration profile is given by:

$$\frac{\partial(\Delta n)}{\partial t} = D\frac{\partial^2(\Delta n)}{\partial r^2} - \frac{\Delta n}{\tau_{\text{volume}}} = -S\Delta n, \tag{35}$$

where S is the surface recombination velocity, D is the diffusion constant and τ_{volume} is the electron lifetime of the bulk material. The solution of this continuity equation gives an exponential time decay of the carrier density with the following carrier lifetime:

$$\frac{1}{\tau} = \frac{1}{\tau_{\text{volume}}} + \frac{4\beta^2 D}{d^2} = \frac{1}{\tau_{\text{volume}}} + \frac{4S}{d}, \tag{36}$$

where d is the NW diameter. This equation can then be fitted to plots of the photoconductivity decay to determine the carrier lifetime and surface recombination velocity of the material.

Furthermore, the effective carrier mobility, $\phi\mu$, can be extracted from the measured value of the photoconductivity and is given by:

$$\phi\mu = \frac{\Delta\sigma_{\mathrm{l,max}}(\omega)A_{\mathrm{eff}}}{\phi} n_{\mathrm{p}} e, \tag{37}$$

where μ is the mobility, A_{eff} is the effective area of the optical pump and THz pulse overlap, ϕ is the photon-to-carrier conversion rate and n_{p} is the photoexcited charge carrier density, which for a sample of thickness d equates to:

$$n_{\mathrm{p}} = \frac{I}{Ed}\left(1 - e^{-d/\alpha}\right), \tag{38}$$

where I is the photoexcitation fluence, E is the photon energy and α is the absorption depth at the excitation wavelength for the material. By taking the peak value of the photoconductivity measured after photoexcitation and calculating the photoexcited carrier density, the effective carrier mobility can then be calculated. It is important to note that as the photon-to-carrier conversion rate is unknown for this method, the effective carrier mobility is a lower limit, which becomes equal to the actual carrier mobility when all photons absorbed are converted to free charge carriers. The effective carrier mobility is also a sum of the carrier mobilities for both electrons and holes, as the two contributions cannot be separated. From this effective carrier mobility, the carrier scattering rate, mean free path, diffusion constant and length can then be obtained from the following equations respectively:

$$\begin{aligned} \mu &= \frac{e\tau}{m^*}, \\ \lambda_{\mathrm{mfp}} = v\tau &= (\sigma n)^{-1}, \\ D &= \frac{k_{\mathrm{b}} T \mu}{e}, \\ L &= (D\tau)^{1/2}, \end{aligned} \tag{39}$$

where τ is the carrier scattering rate, λ_{mfp} the mean free path, D the diffusion constant, L the diffusion length, $k_{\mathrm{b}} = 1.38 \times 10^{-23}\mathrm{JK}^{-1}$ is the Boltzmann constant and v is the average carrier velocity. Thus, numerous key transport parameters can be determined from extraction of the photoconductivity from OPTP measurements.

Fitting to Photoconductivity Spectra

The complex photoconductivity of a free carrier plasma with a plasmon resonance can be described by the following equation:

$$\Delta\sigma\left(n, m^*, \gamma\right) = \frac{ine^2\omega}{m^*\left(\omega^2 - \omega_0^2 + i\omega\gamma\right)}, \tag{40}$$

where n is the carrier density, e is the electronic charge, m_{e}^* is the effective mass of the charge carrier, and γ is the momentum scattering rate. ω_0 is the plasmon resonance frequency given by:

$$\omega_0(n, m^*) = \sqrt{\frac{gne^2}{m^*\epsilon_{\mathrm{r}}\epsilon_0}}, \tag{41}$$

where ϵ_{r} is the dielectric constant of GaAs nanowires at terahertz frequencies, ϵ_0 is the permittivity of free space, and g is a constant that depends on the nanowire geometry and

surrounding dielectric medium.[8] In order to account for any unintentional doping within the samples, the photoconductivity expression must be modified, as there is a charge carrier density present without photoexcitation that produces its own plasmon response.[6,9,10] It is important to note that for InAs nanowires, the hole conductivity is expected to be negligible due to the donor-like nature of the surface states in InAs nanowires. Therefore, for the purposes of these samples, the photoconductivity expression can expressed as:

$$\Delta\sigma = \frac{ie^2\omega}{m_{\mathrm{e}}^*}\left[\frac{n_{\mathrm{total}}}{\omega^2 - \{\omega_0(n_{\mathrm{total}})\}^2 + i\omega\gamma} - \frac{n_{\mathrm{d}}}{\omega^2 - \{\omega_0(n_{\mathrm{d}})\}^2 + i\omega\gamma}\right], \tag{42}$$

where $n_{\mathrm{total}} = n_{\mathrm{photo}} + n_{\mathrm{d}}$ is the sum of the photoexcited and donated electon density.

For each sample, a global fitting routine was applied to all the photoconductivity spectra at various photoexcitation fluences with g fixed to 0.25.[11] n_{d} was set to a global parameter, remaining constant for all spectra, whereas n_{p} and γ_e were allowed to vary as local parameters for each spectrum, as the photoexcited electron density and scattering rates vary with photoexcitation fluence. Bulk values for InAs of $0.023m_{\mathrm{e}}$, $0.41m_{\mathrm{e}}$ and 15.15 were used for m_{e}^*, m_{h}^* and ϵ_{r} respectively **add a citation**. The solid lines in Figures 3 and 4 in the main manuscript represent the fits for Equation 42 with the measured photoconductivity spectra, showing excellent agreement for all samples. From these fits, the carrier mobilities and extrinsic carrier concentrations were extracted.

Full Temperature Dependence of Terahertz Photoconductivity Spectra and Raman Spectra for $InAs_{0.65}Sb_{0.35}$ and InAs Reference Nanowires

Figure 3 shows the full temperature dependence of terahertz photoconductivity spectra for both the InAs reference nanowires and $InAs_{0.65}Sb_{0.35}$ nanowires taken at 5 ps after pho-

toexcitation at a fluence of $190\,\mu\,\mathrm{J\,cm^{-2}}$. As explained in the main manuscript, all spectra show a clear Lorentzian response with the plasma frequency falling at the point where the imaginary part of the photoconductivity crosses the x-axis. As the temperature is decreased, a narrowing in this Lorentzian response along with a slight red-shift in the plasma frequency is observed. This is indicative of an increase in mobility and decrease in carrier concentration with decreasing temperature, as expected.

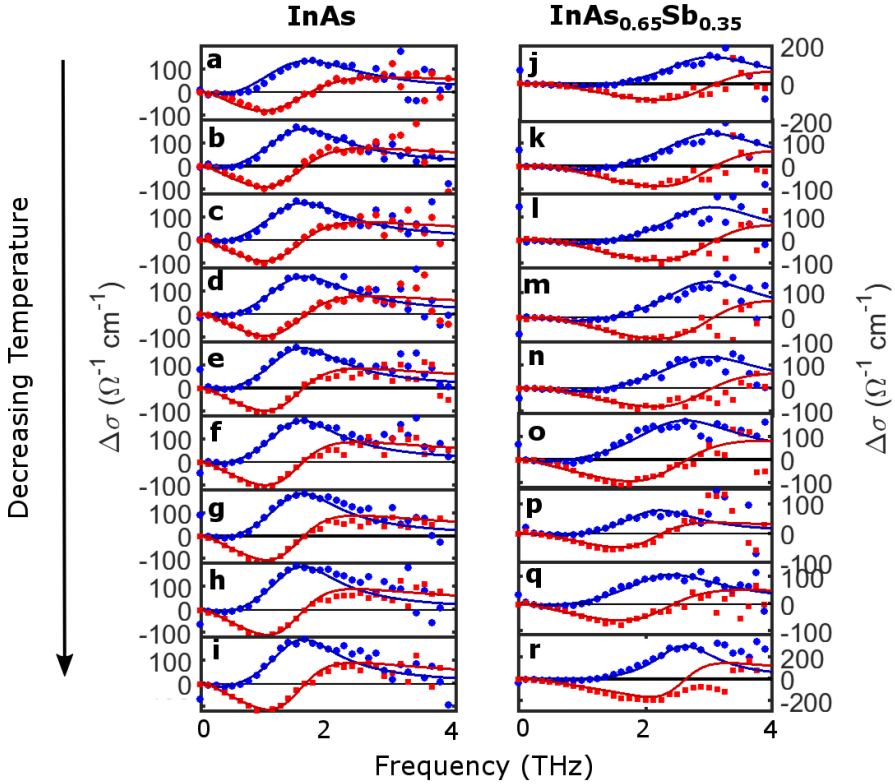

Figure 3: Real (blue) and imaginary (red) part of the photoconductivity taken at 5 ps after photoexcitation at a fluence of $244\,\mu\,\mathrm{J\,cm^{-2}}$ as a function of frequency for (a-i) the InAs reference nanowires and (j-r) the $InAs_{0.65}Sb_{0.35}$ nanowires. Spectra are presented in order of decreasing temperature: (a,j) 300 K, (b,k) 260 K, (c,l) 220 K, (d,m) 180 K, (e,n) 140 K, (f,o) 80 K, (g,p) 50 K, (h,q) 30 K and (i,r) 10 K.

Figure 4 shows the full temperature dependence of the Raman spectra for a single InAs reference nanowire and a single $InAs_{0.65}Sb_{0.35}$ nanowire. The nanowires were photoexcited at an average power of 250μW at an excitation wavelength of 488 nm. As seen in the main manuscript, a coupled LOPCM mode is observed, with the contributions of this coupled mode displayed by the solid blue lines. Similar to the THz measurements, a narrowing of

the LOPCM mode accompanied by a red-shift with decreasing temperature is exhibited, indicating an increases in mobility and decrease in carrier concentration respectively.

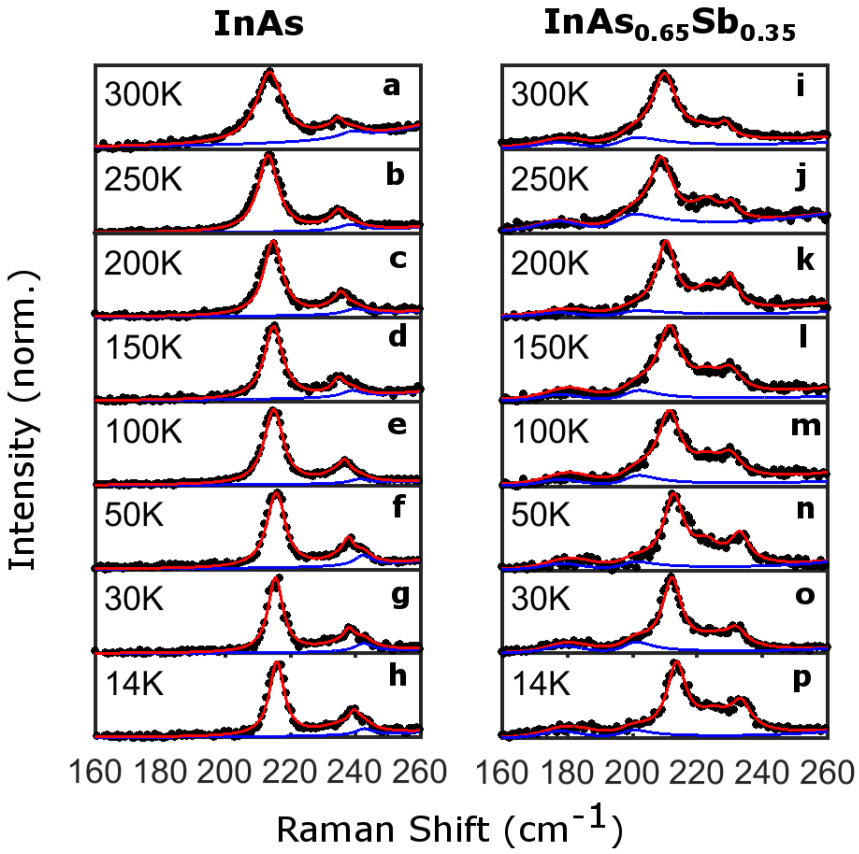

Figure 4: Raman intensity as a function of Raman shift for (a-h) the InAs reference nanowires and (i-p)the $InAs_{0.65}Sb_{0.35}$ nanowires. Spectra were taken for a single nanowire excited at 488nm with an average power of 250μW. The red line represents a Lorentzian fit for the TO and LO modes, where the blue line represents the fit for the LOPCM mode. The spectra are presented in order of decreasing temperature as follows: (a,i) 300 K, (b,j) 250 K, (c,k) 200 K, (d,l) 150 K, (e,m) 100 K, (f,n) 50 K, (g,o) 30 K, and (h,p) 14 K.

Acknowledgement

The authors thank the EPSRC (U.K.) and European Research Council (ERC) under the European Union's Horizon 2020 research and innovation programme (grant agreement 675867), as well as the Swiss National Science Foundation via projects nr137648 and 156081

References

(1) Potts, H.; Friedl, M.; Amaduzzi, F.; Tang, K.; Tütüncüoglu, G.; Matteini, F.; Alarcon Lladó, E.; McIntyre, P. C.; Fontcuberta i Morral, A. *Nano Letters* **2016**, *16*, 637–643.

(2) Amaduzzi, F.; Alarcón-Lladó, E.; Hautmann, H.; Tanta, R.; Matteini, F.; Tütüncüolu, G.; Vosch, T.; Nygård, J.; Jespersen, T.; Uccelli, E. *Journal of Physics D: Applied Physics* **2016**, *49*, 095103.

(3) Hon, D. T.; Faust, W. L. *Applied Physics* **1968**, *1*, 241–256.

(4) Cuscó, R.; Alarcón-Lladó, E.; Artús, L.; Hurst, W. S.; Maslar, J. E. *Phys. Rev. B* **2010**, *81*, 195212.

(5) Nowak, U.; Richter, W.; Sachs, G. *physica status solidi (b)* **1981**, *108*, 131–143.

(6) Joyce, H. J.; Boland, J. L.; Davies, C. L.; Baig, S. A.; Johnston, M. B. *Semiconductor Science and Technology* **2016**, *31*, 1–21.

(7) Landauer, R.; Watson, T. J. Electrical conductivity in inhomogeneous media. American Institute of Physics. 1978; pp 1–45.

(8) Parkinson, P.; Lloyd-Hughes, J.; Gao, Q.; Tan, H. H.; Jagadish, C.; Johnston, M. B.; Herz, L. M. *Nano Letters*

(9) Boland, J. L.; Conesa-Boj, S.; Parkinson, P.; Tütüncüoglu, G.; Matteini, F.; Rüffer, D.; Casadei, A.; Amaduzzi, F.; Jabeen, F.; Davies, C. L.; Joyce, H. J.; Herz, L. M.; Fontcuberta i Morral, A.; Johnston, M. B. *Nano Letters* **2015**, *15*, 1336–1342.

(10) Gül, Ö.; Van Woerkom, D. J.; van Weperen, I.; Car, D.; Plissard, S. R.; Bakkers, E. P.; Kouwenhoven, L. P. *Nanotechnology* **2015**, *26*, 215202.

(11) Joyce, H. J.; Wong-Leung, J.; Yong, C.; Docherty, C. J.; Paiman, S.; Gao, Q.; Tan, H. H.; Jagadish, C.; Lloyd-Hughes, J.; Herz, L. M.; Johnston, M. B. *Nano Letters* **2012**, *12*, 5325–5330.